

Efficient manipulation of terahertz waves by multi-bit coding metasurfaces and further applications of such metasurfaces

Yunping Qi(祁云平)† Baohe Zhang(张宝和), Jinghui Ding(丁京徽), Ting Zhang(张婷), Xiangxian Wang(王向贤), and Zao Yi(易早)

Citation: Chin. Phys. B, 2021, 30 (**2**): 024211. DOI: 10.1088/1674-1056/abd6fc
Journal homepage: http://cpb.iphy.ac.cn; http://iopscience.iop.org/cpb

What follows is a list of articles you may be interested in

Hybrid vector beams with non-uniform orbital angular momentum density induced by designed azimuthal polarization gradient

Lei Han(韩磊), Shuxia Qi(齐淑霞), Sheng Liu(刘圣), Peng Li(李鹏), Huachao Cheng(程华超), Jianlin Zhao(赵建林)
Chin. Phys. B, 2020, 29 (**9**): 094203. DOI: 10.1088/1674-1056/aba09d

Hyperbolic metamaterials for high-efficiency generation of circularly polarized Airy beams

Lin Chen(陈林), Huihui Li(李会会), Weiming Hao(郝玮鸣), Xiang Yin(殷祥), Jian Wang(王健)
Chin. Phys. B, 2020, 29 (**8**): 084210. DOI: 10.1088/1674-1056/ab96a1

Comparison of three kinds of polarized Bessel vortex beams propagating through uniaxial anisotropic media

Jia-Wei Liu(刘佳伟), Hai-Ying Li(李海英), Wei Ding(丁炜), Lu Bai(白璐), Zhen-Sen Wu(吴振森), Zheng-Jun Li(李正军)
Chin. Phys. B, 2019, 28 (**9**): 094214. DOI: 10.1088/1674-1056/ab37f5

Pancharatnam-Berry metasurface for terahertz wave radar cross section reduction

Shao-He Li(李绍和), Jiu-Sheng Li(李九生)
Chin. Phys. B, 2019, 28 (**9**): 094210. DOI: 10.1088/1674-1056/ab33f5

A method for generating double-ring-shaped vector beams

Huan Chen(陈欢), Xiao-Hui Ling(凌晓辉), Zhi-Hong Chen(陈知红), Qian-Guang Li(李钱光), Hao Lv(吕昊), Hua-Qing Yu(余华清), Xu-Nong Yi(易煦农)
Chin. Phys. B, 2016, 25 (**7**): 074201. DOI: 10.1088/1674-1056/25/7/074201

Efficient manipulation of terahertz waves by multi-bit coding metasurfaces and further applications of such metasurfaces*

Yunping Qi(祁云平)[1,†] Baohe Zhang(张宝和)[1], Jinghui Ding(丁京徽)[1], Ting Zhang(张婷)[1], Xiangxian Wang(王向贤)[2], and Zao Yi(易早)[3]

[1] College of Physics and Electronic Engineering, Northwest Normal University, Lanzhou 730070, China
[2] School of Science, Lanzhou University of Technology, Lanzhou 730050, China
[3] Joint Laboratory for Extreme Conditions Matter Properties, Southwest University of Science and Technology, Mianyang 621900, China

(Received 16 October 2020; revised manuscript received 17 December 2020; accepted manuscript online 28 December 2020)

Benefiting from the unprecedented superiority of coding metasurfaces at manipulating electromagnetic waves in the microwave band, in this paper, we use the Pancharatnam–Berry (PB) phase concept to propose a high-efficiency reflective-type coding metasurface that can arbitrarily manipulate the scattering pattern of terahertz waves and implement many novel functionalities. By optimizing the coding sequences, we demonstrate that the designed 1-, 2-, and 3-bit coding metasurfaces with specific coding sequences have the strong ability to control reflected terahertz waves. The two proposed 1-bit coding metasurfaces demonstrate that the reflected terahertz beam can be redirected and arbitrarily controlled. For normally incident x-and y-polarized waves, a 10 dB radar cross-section (RCS) reduction can be achieved from 2.1 THz to 5.2 THz using the designed 2-bit coding metasurface. Moreover, two kinds of orbital angular momentum (OAM) vortex beams with different moduli are generated by a coding metasurface using different coding sequences. Our research provides a new degree of freedom for the sophisticated manipulation of terahertz waves, and contributes to the development of metasurfaces towards practical applications.

Keywords: coding metasurface, Pancharatnam–Berry phase, multiple beams, radar cross-section (RCS) reduction, orbital angular momentum

PACS: 42.68.Mj, 81.05.Xj, 42.25.Ja, 78.67.Pt **DOI:** 10.1088/1674-1056/abd6fc

1. Introduction

Terahertz (THz) waves, whose frequency range is between 0.1 THz and 10 THz, are on the cutting edge of new technologies and have drawn enormous attention from worldwide academia in recent years, because of their numerous potential applications in biosensing, security imaging, and THz high-speed communications.[1–6] The manipulation of terahertz waves, especially their polarization, phase, and amplitude, is important in terahertz application systems. Unfortunately, most of the conventional materials in nature have great difficulty in achieving effective control of terahertz waves, which limits the development of terahertz technology and applications. Therefore, we need new and innovative ideas to address the lack of natural materials that can be used in the terahertz band.

A metasurface is a two-dimensional planar structure composed of an array of subwavelength units, which provides unprecedented capabilities for the flexible and effective manipulation of the phase, amplitude, polarization, and various other properties of incident electromagnetic waves.[7–17] The arrival of metasurfaces has made up for the shortage of electromagnetic materials in the terahertz band, has provided an effective way to realize functional devices in the terahertz band, and is expected, in essence, to break through the bottleneck of terahertz technology development. To date, many remarkable achievements based on metasurfaces have been accomplished and demonstrated in the microwave band, including high-gain antennas,[18] polarization conversion,[19–21] beam focusing,[22,23] radar cross-section reduction,[24–26] vortex-beam generation,[27–30] and so on. In comparison with the microwave band, terahertz waves are a new research topic, and related technologies are still in the early stages of exploration. More recently, metasurfaces have been extended to the terahertz region and have played an irreplaceable role in the production of novel functionalities, such as near-perfect absorbers,[31–36] super-lenses,[37] holographic imaging,[38,39] and sensing.[40–43] Unfortunately, so far, most of the new achievements with metasurfaces have had problems due to their complex structure, low operating efficiency, and because they can only afford one specific function within a limited frequency range, which is a key challenge for terahertz technology to be able to achieve multiple functionalities.

Digital coding metasurfaces are a significant branch of metasurfaces that create a new bridge between the physical world and digital information science. In this study, to the best

*Project supported by the National Natural Science Foundation of China (Grant No. 61865008), Northwest Normal University Young Teachers' Scientific Research Capability Upgrading Program (Grant No. NWNU-LKQN2020-11), and the Scientific Research Fund of Sichuan Provincial Science and Technology Department, China (Grant No. 2020YJ0137).

†Corresponding author. E-mail: qiyunping@nwnu.edu.cn

© 2021 Chinese Physical Society and IOP Publishing Ltd

of our knowledge, this is the first time that the proposed double E-shaped structure has been combined with the PB phase principle to generate a multi-bit coding metasurface, which shows promise for many important applications in the terahertz range. Using a 1-bit coding metasurface with specific distributions of the coding sequences, the reflected terahertz waves can be flexibly and independently manipulated. To realize a low RCS in the terahertz band, we propose a simple and high-performance reflective metasurface based on 2-bit coding elements, which can achieve a >10 dB RCS reduction within a wideband range from 2.1 THz to 5.2 THz. Apart from the useful functionalities described above, we designed two kinds of reflective metasurfaces based on 3-bit coding elements, which were able to realize orbital angular momentum waves with mode numbers of $l=1$ and $l=2$. The simulated results prove that the designed scheme has great potential for future practical application in the terahertz frequency range.

2. Theoretical formulation

To achieve high-efficiency manipulation of incident electromagnetic waves, it is important to obtain 360° full-phase coverage. In terms of controlling the geometric phase change, the PB phase metasurface exhibits unique advantages, and can simply obtain phase responses, just by a rotation of the metallic pattern's angle. In what follows, we first theoretically infer the principle of the PB phase. For a double E-shaped unit under the Cartesian coordinate system, when the optical axis is rotated by an angle of θ in the anticlockwise direction, the coefficients of reflection can be characterized by the reflective Jones matrix[44]

$$\boldsymbol{R}=\begin{bmatrix} R_{xx} & R_{xy} \\ R_{yx} & R_{yy} \end{bmatrix}, \tag{1}$$

in which the diagonal elements R_{xx} and R_{yy} denote the co-polarized reflection coefficients under the normal incidence of x- and y-polarization, whereas the off-diagonal elements, R_{xy} and R_{yx}, denote the cross-polarized reflection coefficients under the normal incidence of x- and y-polarization. In general, for an anisotropic metasurface at an oblique incidence, $R_{xy}\neq R_{yx}$. In the case of normal incidence, i.e., $R_{xy}=R_{yx}=0$, the reflection matrix has the following relationship in the rectangular coordinate system:

$$\begin{aligned}\boldsymbol{R}^{\theta}_{\text{rotate}}&=\boldsymbol{T}(-\theta)\cdot\begin{bmatrix} R_{xx} & 0 \\ 0 & R_{yy} \end{bmatrix}\cdot T(\theta)\\ &=\begin{bmatrix} R_{xx}\cos^2(\theta)+R_{yy}\sin^2(\theta) & (R_{yy}-R_{xx})\sin(\theta)\cos(\theta) \\ (R_{yy}-R_{xx})\sin(\theta)\cos(\theta) & R_{xx}\sin^2(\theta)+R_{yy}\cos^2(\theta) \end{bmatrix},\end{aligned} \tag{2}$$

where $\boldsymbol{T}(\theta)=\begin{bmatrix} \cos\theta & -\sin\theta \\ \sin\theta & \cos\theta \end{bmatrix}$ means the rotation matrix of the rectangular coordinate system rotated by an angle θ in the counterclockwise direction. In the case of incident circularly polarized waves, the reflection matrix can be written as

$$\boldsymbol{R}^{\theta}_{\text{LR}}=\frac{1}{2}\begin{bmatrix} 1 & -\text{j} \\ 1 & \text{j} \end{bmatrix}R^{\theta}_{\text{rotate}}\begin{bmatrix} 1 & -\text{j} \\ 1 & \text{j} \end{bmatrix}^{-1}. \tag{3}$$

By substituting Eq. (2) into Eq. (3), the reflection matrix under the excitation of a circularly polarized wave can be derived as

$$\begin{cases} r_{\text{LR}}=\frac{1}{2}\left[(r_{xx}+r_{yy})+\text{j}(r_{xy}-r_{yx})\right], \\ r_{\text{RL}}=\frac{1}{2}\left[(r_{xx}+r_{yy})-\text{j}(r_{xy}-r_{yx})\right], \\ r_{\text{LL}}=\frac{1}{2}\left[(r_{xx}-r_{yy})-\text{j}(r_{xy}+r_{yx})\right]\text{e}^{-\text{j}2\theta}, \\ r_{\text{RR}}=\frac{1}{2}\left[(r_{xx}-r_{yy})+\text{j}(r_{xy}+r_{yx})\right]\text{e}^{\text{j}2\theta}, \end{cases} \tag{4}$$

where r_{LL} and r_{RR} represent co-polarized reflection coefficients under the normal incidence of left and right circular polarization, respectively, and r_{LR} and r_{RL} represent cross-polarized reflection coefficients under the normal incidence of left and right circular polarization, respectively. From Eq. (4) we find that there are two components, r_{LL} and r_{RR}, that carry the PB phase $\text{e}^{\pm\text{j}2\theta}$, which is twice the metasurface coding element rotational angle θ, while the other two components r_{LR} and r_{RL} have no phase difference when $|r_{xy}|\approx|r_{yx}|\approx 1$ and $|r_{xx}|\approx|r_{yy}|\approx 0$. The above analysis shows that the phase responses are easily achieved by regularly rotating the metal patterns to different angles of orientation, which simplifies the process of designing the coding metasurface.

Our target in this work is to achieve efficient manipulation of terahertz waves, RCS reduction, and OAM generation by appropriate arrangement of the coding sequence. The key step is to achieve a phase shift that covers a broad range of 0°–360° while maintaining constant scattering amplitudes. To accomplish our goal, the rotation angle θ of each coding particle is changed from 0° to 157.5° in steps of 22.5°. The corresponding phases of the eight coding particles are 0°, 45°, 90°, 135°, 180°, 225°, 270°, and 315°, respectively. Because each coding particle has a specific rotational angle, there is an additional degree of freedom for manipulating terahertz waves that offers many novel functionalities.

3. Design of the unit and theoretical analysis

In the design of our PB coding metasurface, the basic coding particle unit is a classic sandwich structure, which consists of three parts: a top-layer double E-shaped structure, an intermediate dielectric layer, and a bottom metal layer, as shown in Fig. 1(a). The double-E structure and the bottom metallic film are made of copper, whose conductivity and thickness are 5.8×10^7 S/m and 240 nm, respectively. Polyimide is adopted as the intermediate dielectric substrate with a thickness of $t=11$ μm and the relative dielectric constant and loss tangent are $\varepsilon_{\text{r}}=3.0$ and $\tan\delta=0.001$, respectively. The detailed geometric parameters of the coding particle were optimized by simulation software as follows: $a=20$ μm, $b=15$ μm,

$c = 10$ μm, $w = 2.5$ μm, $g = 4$ μm. The period of the coding particle is $p_x = p_y = 36$ μm. Unit-cell simulation was performed using the finite element method, in which the master and slave boundary conditions were used in the x and y directions and Floquet port excitation was adopted in the $-z$ direction.

To understand the polarization characteristics of the double E-shaped designed metasurface in more detail, the co- and cross- polarized reflection coefficients under the normal incidence of circularly polarized waves were calculated using the finite element method (FEM). Fig. 1(b) shows the calculated results for the cross-polarized r_{LR} (r_{RL}) and co-polarized r_{LL} (r_{RR}) reflection coefficients in the frequency range from 2.1 THz to 5.2 THz, under the normal incidence of LCP and RCP waves. It is obvious that over a broad frequency range from 2.34 THz to 4.77 THz, the cross-polarized reflection coefficients are higher than -1 dB and the co-polarized reflection coefficients are very low, reaching -45 dB under the normal incidence of LCP or RCP waves. It is evident that our design can be used to achieve high-efficiency polarization conversion. The polarization conversion ratio (PCR) is defined as follows:[45] $\mathrm{PCR_L} = |r_{RL}|^2/\left(|r_{RL}|^2 + |r_{LL}|^2\right)$. We calculated the $\mathrm{PCR_L}$ for incident LCP excitation, as shown in Fig. 1(c), which shows that the $\mathrm{PCR_L}$ is larger than 90% within a frequency range from 2.3 THz to 4.65 THz. One important phenomenon can be found in Fig. 1(d): the reflection amplitudes of the coding particle are almost consistent over the entire frequency range under the normal incidence of x- and y-polarized waves. At the same time, within a wider frequency band, the reflected phase difference between the x- and the y-polarized incidences is almost a constant 180°, which ensures that multiple functions of the coding metasurface can be achieved at the operating frequency.

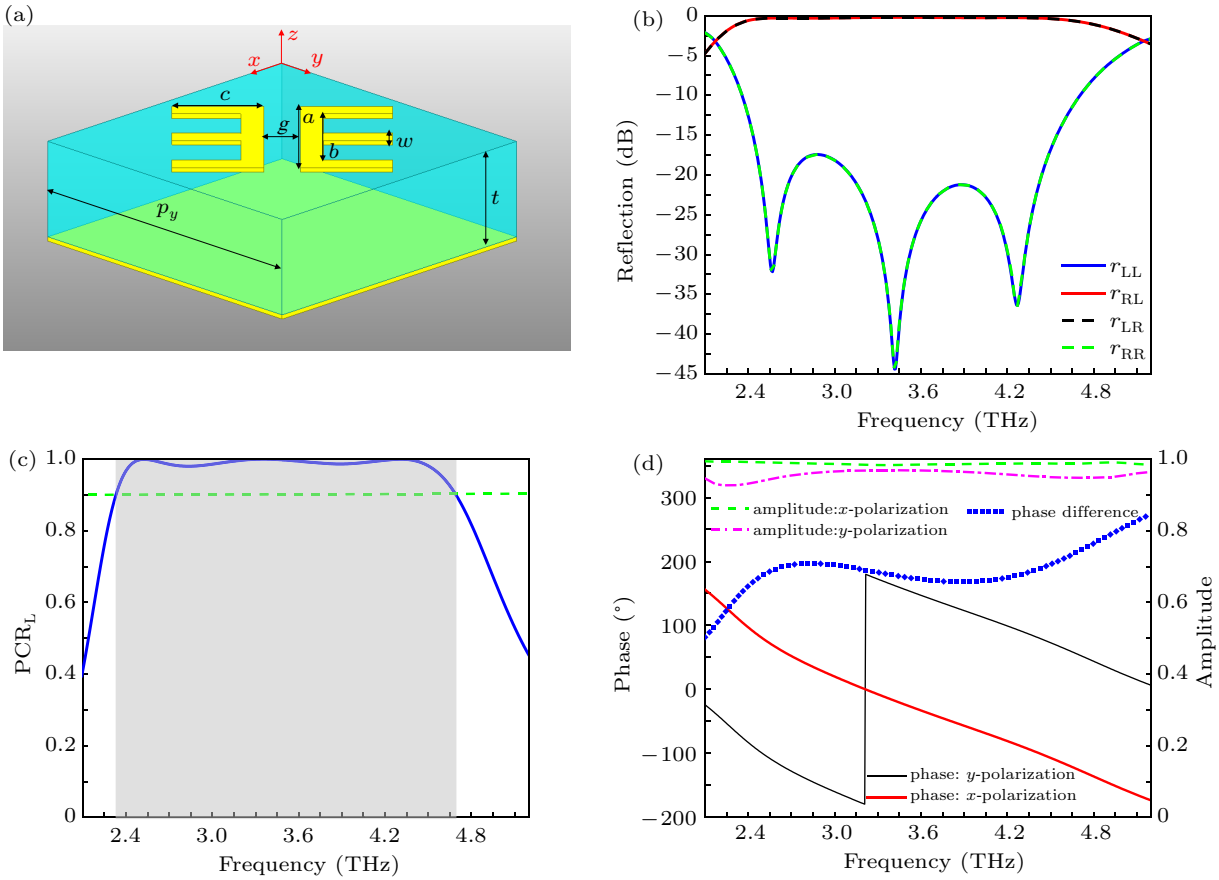


Fig. 1. (a) Design of the double Eshaped basic coding cell. (b) Simulated co- and cross-polarized reflection coefficients under the normal incidence of LCP and RCP waves. (c) Simulated PCR under LCP wave excitation. (d) Simulated reflected phase and amplitude under the normal incidence of linearly x- and y-polarized waves, respectively.

By adopting the concept of the PB phase, the required phase can be more conveniently achieved and the scattering patterns of the coding metasurface can be deflected in a specific direction. Figure 2(a) shows the particles of the 1-bit, 2-bit, and 3-bit coding metasurfaces and the corresponding relationship between the particle and the rotation angle. For simplicity, the numbers "0" to "7" represent the bit combinations "000", "001", "010", "011", "100", "101", "110", and "111", respectively. Figure 2(b) depicts the magnitude of the reflection response for cross-polarization of eight basic coding particles with different rotational angles under the incidence of LCP or RCP waves. One can find that as the rotation angle θ changes from 0° to 157.5° with steps of 22.5°, the amplitude of the cross-polarization reflection coefficient for eight el-

ements is greater than 90% over a broadband frequency range from 2.4 THz to 4.7 THz. Figures 2(c) and 2(d) show the phase responses of eight basic coding elements under the normal incidence of LCP and RCP waves, respectively. It is worth noting that in the frequency range from 2.1 THz to 5.2 THz, the phase difference between adjacent coding elements always remains at about 45°, which not only ensures that our design of PB coding metasurface can work over a wide frequency range but also proves the corresponding relationship between the reflection's phase difference and unit cell's rotational angle is $\pm 2\theta$, where "+" corresponds to LCP wave incidence and "−" corresponds to RCP wave incidence.

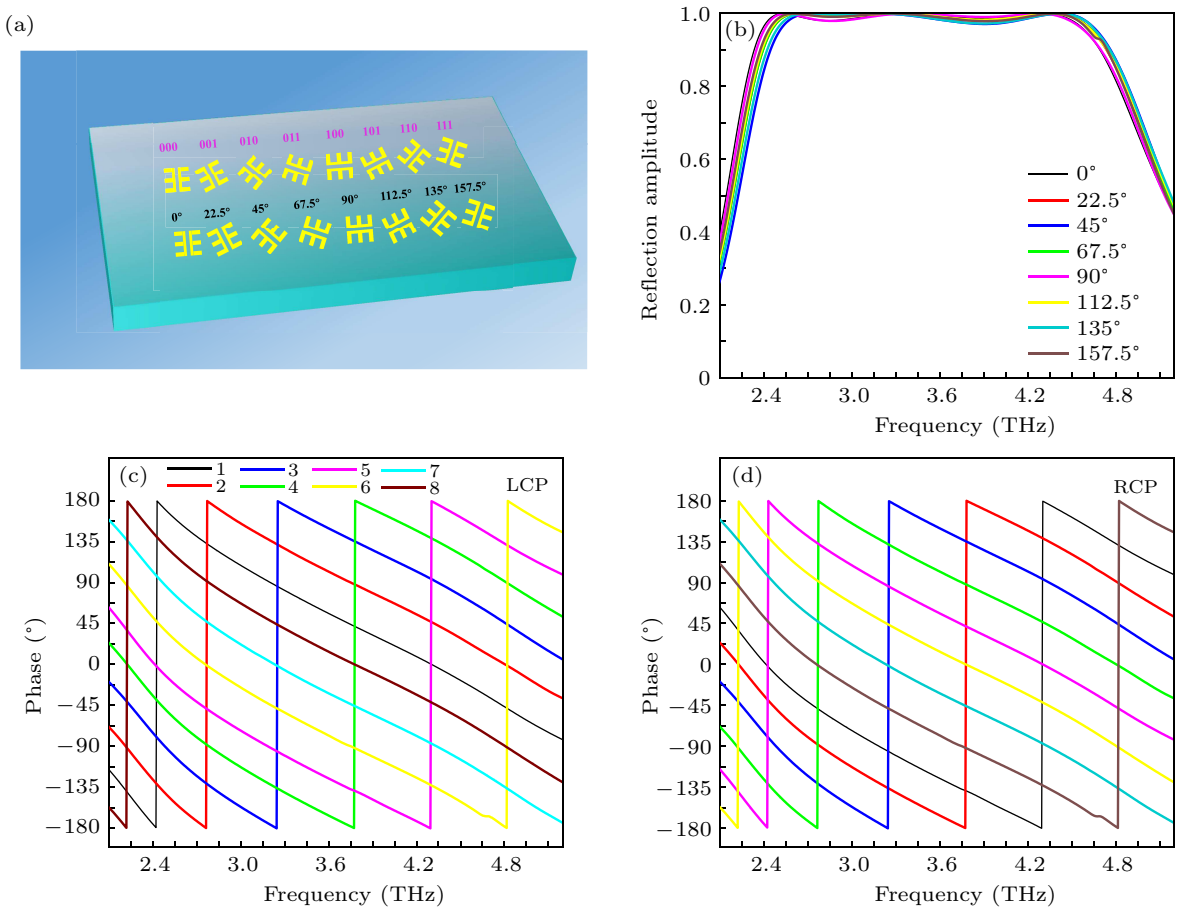


Fig. 2. (a) The design of the coding elements for 1-, 2-, and 3-bit coding metasurfaces. (b) The corresponding reflected amplitude of cross-polarization with different rotation angles. The simulated reflection phase responses of the basic element with different rotation angles for (c) LCP and (d) RCP incidences.

By designing appropriate coding sequences, the multi-bit coding metasurface provides new opportunities for the effective manipulation of terahertz-wave scattering patterns and may offer widespread applications. In the next sections, we will give a few examples to illustrate that multi-bit coding metasurfaces have the ability to achieve highly efficient manipulation of terahertz waves and that they can implement different functions.

3.1. The 1-bit coding metasurface

For a 1-bit coding metasurface, the basic coding elements are composed of two digital states, "0" and "1", and their corresponding reflection phases are 0° and 180°, respectively. It is well known that lots of interesting physical phenomena of electromagnetic regulation mechanisms can be generated by arranging specific coding sequences. In other words, we can control the scattering characteristics of coding metasurfaces by changing the corresponding "0" and "1" coding sequences. As an example, two kinds of 1-bit coding metasurfaces are employed with different coding sequences to verify that the coding metasurface has properties that can control far-field scattering patterns more freely. For the 1-bit coding metasurface M_1, the simulated three-dimensional scattering patterns under the normal incidence of an LCP wave at 3 THz are shown in Fig. 3(a). It should be noted that when the coding sequences "00001111⋯" of the metasurface M_1 are arranged in the x-axis direction, two symmetrical main beams with angles of $\theta_r = 20.3°$ are generated. According to a generalization of Snell's law, the anomalous reflection angle for normal incidence can be predicted by the following equation:[46]

$$\theta_r = \arcsin(\lambda/\Gamma), \tag{5}$$

in which λ is the free-space wavelength of the incident wave at 3 THz and $\Gamma = 4 \times 144$ μm represents the period of the cod-

ing sequence. Similarly, we also design the M_2 coding metasurface with the "010101···/101010···" coding sequence, as displayed in Fig. 3(b). In this case, each lattice consists of 3×3 units of the same "0" or "1" coding elements. It can be observed that the scattered energy for a normally incident LCP wave at 3 THz is equally split into four symmetrical oblique beams with the same elevation angle. The elevation angle θ and the azimuthal angle φ of the four oblique beams can be predicted by the following equations:[47,48]

$$\theta = \arcsin\left(\sqrt{\sin^2\theta_1 + \sin^2\theta_2}\right), \tag{6}$$

$$\varphi = \arctan\left(\frac{\sin\theta_2}{\sin\theta_1}\right), \tag{7}$$

in which θ_1 and θ_2 are the beam deviation angles corresponding to the two periodic coding sequences that vary along the x and y directions, respectively. Under such conditions, θ_1 and θ_2 as calculated by Eq. (5) are both 27.6°, and thus, the new beam deviation angle is calculated to be 40.5°. The azimuthal angles φ of the four oblique beams are 45°, 135°, 225°, and 315°, respectively. The numerical simulation and theoretical calculation are in excellent agreement, which proves the outstanding performance of the proposed schemes. To further verify this interesting phenomenon, the near-field distributions of the two proposed coding metasurfaces are analyzed, as depicted in Figs. 3(c) and 3(d). In addition, the two-dimensional scattering patterns are also studied, as illustrated in Figs. 3(e) and 3(f). The above research results demonstrate that our designed coding metasurface has good performance when used to manipulate the energy of the main lobe of normally incident terahertz waves, which can be used to realize many interesting applications such as terahertz beam splitters.

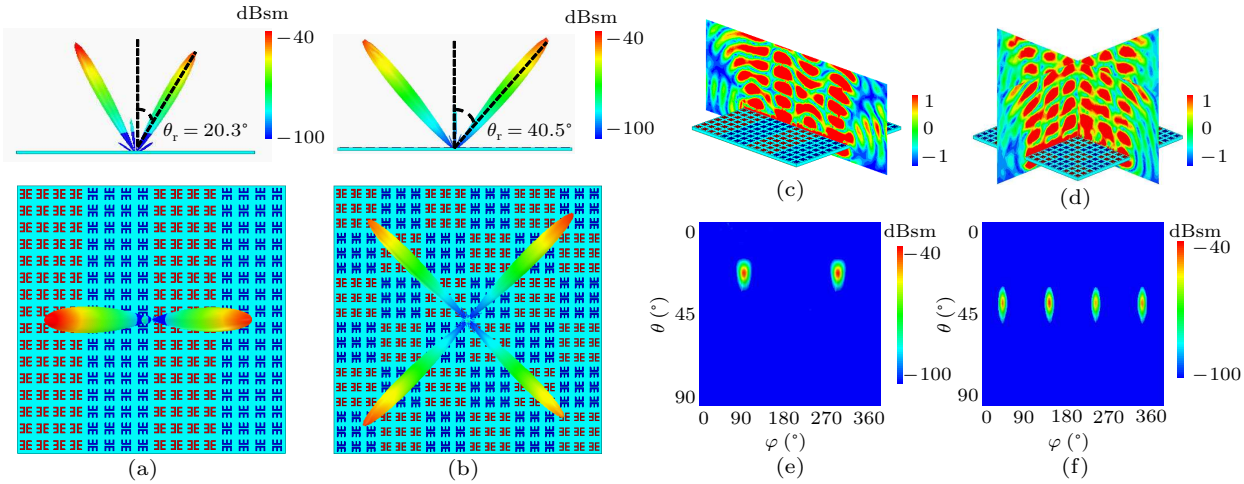


Fig. 3. The simulated 3D and 2D far-field scattering patterns of the 1-bit coding metasurface. (a), (c), (e) The far-field scattering pattern and near-field energy distributions of the 00001111··· sequence at 3 THz. (b), (d), (f) The far-field scattering pattern and near-field energy distributions of the 010101···/101010··· sequence at 3 THz.

3.2. The 2-bit coding metasurface

For a 2-bit coding metasurface, the basic coding particles are composed of four digital states: "0", "2", "4", and "6", whose reflection responses have the same amplitudes and where the phase difference between adjacent digital states is fixed at 90° . Compared with the 1-bit coding metasurface mentioned above, this metasurface offers more abundant phase conditions and higher flexibility for the design of coding sequences. To evaluate the performance of the 2-bit coding metasurface for RCS reduction, a new coding metasurface Ms_1 is optimized and elaborately arranged using 2-bit elements, as shown in Fig. 4. To start with, the key step is to arrange four "0", "2", "4" and "6" elements as an S_1 coding sequence in the x-axis direction. Secondly, we rotate the designed S_1 coding sequence by 90° around the geometric center, as depicted in Fig. 4(a). Finally, the Ms_1 coding metasurface is composed of four arrays, as sketched in Fig. 4(b). In order to observe the scattering behavior, the Ms_1 coding metasurface is simulated using the finite element method. The three-dimensional (3D) scattering patterns of the Ms_1 coding metasurface under plane wave excitation at 4 THz are shown in Fig. 4(c). From the calculated (3D) scattering patterns, one can see that most of the incident electromagnetic energy is distributed in multiple different directions, which has potential applications for stealth. The monostatic RCS is contrasted with the same size of metal ground in Fig. 4(d). It is obvious that the coding metasurface array has better RCS reduction. In order to further validate the reduction efficiency of RCS over a wide band, the relationship between RCS and frequencies ranging from 2.1 TH to 5.2 THz was calculated under normally incident x- and y-polarized waves, as illustrated in Fig. 4(e). The black solid line is the theoretical monostatic RCS of a metallic plate with the same size as the coding metasurface M_{S1}. The result is calculated using the formula:[49] $\mathrm{RCS} = 10 \times \log_{10}\left(4\pi L^4/\lambda^2\right)$, where L is the physical length of the square metallic plate and the λ is the working wave-

length. Compared with the simulated results for the metallic plate, one can note that a tiny deviation exists between the theoretical results for the metal-plate RCS and the simulated value, and that the deviation increases with an increase of frequency. The purple and blue dot–dashed lines denote the simulated results for Ms_1 under normally incident x- and y-polarized waves, respectively. It can be observed that the RCS is reduced by more than 10 dB over the whole working frequency band, which demonstrates that the designed M_{S1} can offer good RCS reduction.

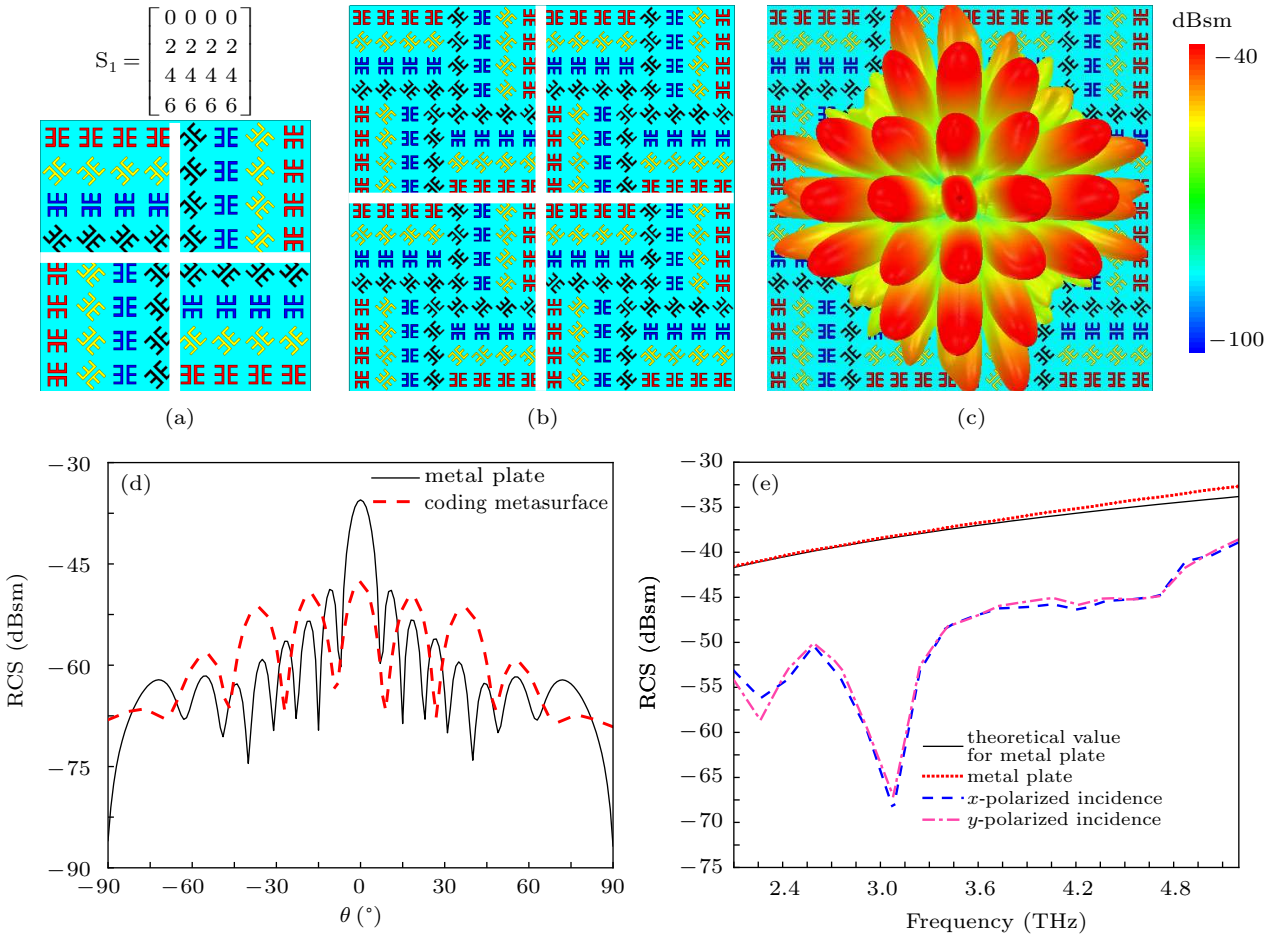


Fig. 4. Schematic diagram of a 2-bit coding metasurface. (a) 8×8 coding sequences. (b) Ms_1 coding array. (c) Simulated 3D scattering patterns of Ms_1 under normally incident plane wave excitation at 4 THz. (d) Simulated monostatic RCSs of Ms_1 and a metal plate at 4 THz for $\varphi = 0$. (e) The monostatic RCS reduction curves for Ms_1 and the equal-sized metal plate under normally incident x-and y-polarized waves.

3.3. The 3-bit coding metasurface

In this section, similarly to the design methods mentioned above for the 1-bit and 2-bit coding metasurfaces, we further introduce a 3-bit coding metasurface, whose basic digital elements are "1", "2", "3", "4", "5", "6", "7", "8", corresponding to phase responses of 0°, 45°, 90°, 135°, 180°, 225°, 270°, and 315°, respectively, which can provide more abundant phases to manipulate terahertz waves. To demonstrate the versatility of the 3-bit coding metasurface for terahertz modulation, two different reflective metasurfaces are employed to generate terahertz vortex beams under the illumination of plane terahertz waves at 3 THz. The numerical calculation is performed by the finite-element method. A typical characteristic of a vortex beam is that it has a spatially distributed spiral phase term $e^{il\varphi}$, where l denotes the designed OAM mode number, also known as the number of topological changes, and φ denotes the azimuthal angle.[50–52] The overall size of the two designed reflective metasurfaces is set to 720×720 μm^2, and they consist of an array of 20×20 cells. For the OAM mode $l = 1$, the metasurface consists of eight sectors, and the phase gradient increment between adjacent sectors is 45°, as shown in Fig. 5(a). For the OAM mode $l = 2$, the metasurface also consists of eight sectors, and the phase gradient increment between adjacent sectors is 90°, as shown in Fig. 5(e). Figures 5(b), 5(f) and 5(c), 5(g) give the simulated results and schematic diagrams of the vortex intensity and phase distribution of $l = 1$ and $l = 2$, respectively. As can be seen from Figs. 5(b) and 5(f), the center point of the light field is a dark field, in other words, the intensity at the vortex's center is zero. As can be seen from the near-field phase distribution of Figs. 5(c) and 5(g), for the $l = 1$ mode, the wave-front's phase exhibits a single spiral state; for the $l = 2$ mode, the wave-front's phase exhibits a double spiral state. It is worth noting that the rotational center of the phase distribution of

the vortex beam is slightly separated, which is caused by the discontinuity of the array's arrangement. The simulated 3D far-field scattering patterns of OAM vortex beams with mode numbers $l = 1$ and $l = 2$ are shown in Figs. 5(d) and 5(h). In addition, the two-dimensional scattering patterns corresponding to the two modes in the radar coordinate system and the Cartesian coordinate system are shown in Figs. 5(i) and 5(j). The above simulation results reveal that the vortex beam with orbital angular momentum is produced using the proposed reflective metasurface, which proves that our design has great potential for next generation ultra-high-speed wireless communication systems.

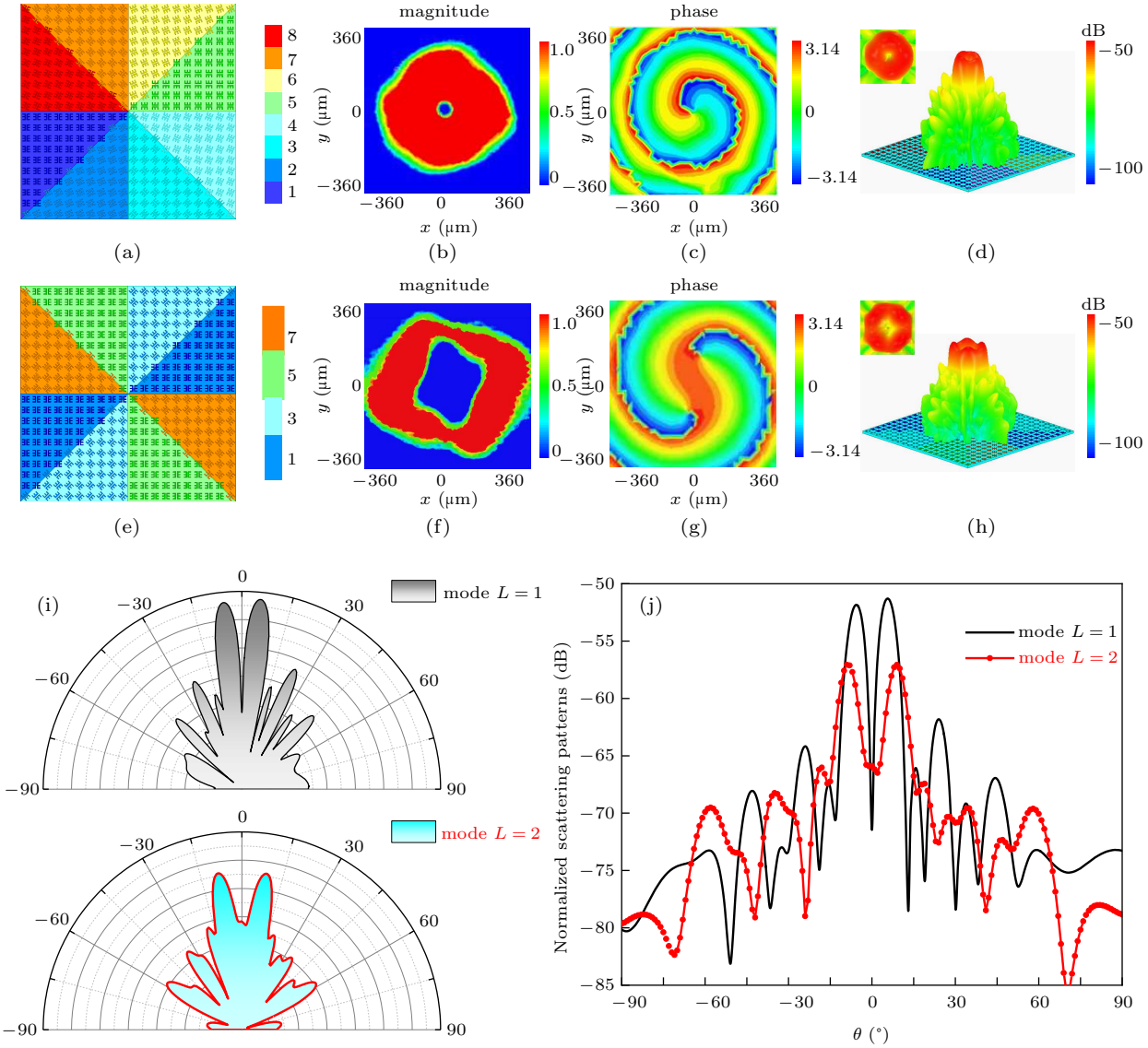


Fig. 5. (a), (e) A schematic diagram of the digital phase distribution used to generate OAM vortex beams with topological charges of $l = 1$ and $l = 2$. (b), (f) The simulated amplitude distributions. (c), (g) The simulated near-field phasedistribution diagram. (d), (h) The simulated 3D far-field scattering patterns. (i), (j) The 2D scattering patterns of the two modes $l = 1$ and $l = 2$.

Finally, although this article is a theoretical and simulative work, and not experimental, the fabrication of coding metasurfaces and experimental demonstration is to be expected: the proposed coding metasurface sample can be manufactured by standard photolithography techniques, electron-beam evaporation equipment, and a lift-off process. The production process is as follows: firstly, a copper film is deposited onto a polyimide film by an electron-beam evaporation coating machine, then a homogenizer is used to evenly apply photoresist to the surface of the sample to be etched. Next, choosing the appropriate temperature and baking time is very important, because the photoresist film can be fully dried after baking the photoresist-spin-coated sample. Secondly, a lift-off process is used to form the metasurface pattern on top of the polyimide layer. Thirdly, the sample is immersed in acetone to remove any excess photoresist. Finally, the sample can be measured by a terahertz time-domain spectroscopic test system.

4. Conclusions

In summary, we have successfully proposed 1-bit, 2-bit, and 3-bit reflection coding metasurfaces to manipulate electro-

magnetic scattering and radiation and to implement different functions, respectively. In our study of the 1-bit coding metasurface, by designing appropriate coding sequences we found that the reflected terahertz wave can be split into two or four main beams, which can be used to realize beam splitting and beam scanning. For RCS-reducing applications, a 2-bit coding metasurface was elaborately designed, which was able to scatter the reflected terahertz energy in more directions. The simulation results showed that the proposed metasurface achieved a >10 dB RCS reduction over a wide frequency band ranging from 2.1 THz to 5.2 THz. In addition, we designed two different kinds of 3-bit coding metasurface for generating multimode OAM beams. The proposed metasurfaces offers new possibilities for terahertz wave control and pave the way for the development of novel functionalities in the future.

References

[1] Ferguson B and Zhang X C 2020 *Nat. Mater.* **1** 26
[2] Song H J and Nagatsuma T 2011 *IEEE Transactions on Terahertz Science and Technology* **1** 256
[3] Jepsen P U, Cooke D G and Koch M 2012 *Laser & Photonics Reviews* **6** 418
[4] Huang S L, Wang X, Chen Y F, Xu J and Mu B Z 2019 *Opt. Express* **27** 337
[5] Grady N K, Heyes J E and Chowdhury D R 2013 *Science* **340** 1304
[6] Nagatsuma T, Ducournau G and Renaud C C 2016 *Nat. Photon.* **10** 371
[7] Zhao R Q, Zheng Z, Dong G H, Lv T T and Zhang H 2019 *Opt. Lett.* **44** 3482
[8] Xu H X, Liu H, Ling X, Sun Y and Yuan F 2017 *IEEE Transactions on Antennas and Propagation* **65** 7378
[9] Zheng Q Q, Li Y, Zhang J, Ma H, Wang J, Pang Y, Han Y, Sui S, Shen Y and Chen Y 2017 *Sci. Rep.* **7** 43543
[10] Saifullah Y, Waqas A B, Yang G and Xu F 2019 *Opt. Express* **28** 1139
[11] Yu Y Z, Xiao F, He C, Jin R and Zhu W 2020 *Opt. Express* **28** 11797
[12] Yin L Z, Huang T J, Han F Y, Liu J Y and Liu P K 2019 *Opt. Lett.* **44** 1556
[13] Dai J Y, Zhao J, Cheng Q and Cui T J 2018 *Light: Science & Applications* **7** 90
[14] Xie X, Pu M P, Liu K P, Jin J J, Ma X L and Luo X G 2019 *Photonics Research* **7** 586
[15] Tao Z, Wan X, Pan B C and Cui T J 2017 *Appl. Phys. Lett.* **110** 121901
[16] Zhang Y, Xie B, Liu W, Cheng H, Chen S and Tian J 2019 *Appl. Phys. Lett.* **114** 091905
[17] Akbari M, Samadi F, Sebak A and Denidni T A 2019 *IEEE Antennas and Propagation Magazine* **61** 40
[18] Zhang L, Wan X, Liu S, Yin J Y, Zhang Q, Wu H T and Cui T J 2017 *IEEE Trans. Antennas Propag* **65** 3374
[19] Li Y J, Li Z W, Liu Y H, Kong Y and Huang L 2019 *Optical Materials* **98** 109420
[20] Qi Y P, Zhang B H, Liu C Q and Deng X Y 2020 *IEEE Access* **8** 116675
[21] Sajjad M, Kong X, Liu S, Ahmed A and Wang Q 2020 *Phys. Lett. A* **384** 126567
[22] Li S H and Li J S 2019 *Chin. Phys. B* **28** 094210
[23] Li H, Wang G, Liang J, Gao X, Hou H and Jia X 2017 *IEEE Transactions on Antennas and Propagation* **65** 1452
[24] Li K, Liu Y, Jia Y and Guo Y 2017 *IEEE Transactions on Antennas & Propagation* **65** 4288
[25] Sharma A, Gangwar D, Kumar Kanaujia B and Dwari S 2018 *AEU - International Journal of Electronics and Communications* **91** 132
[26] Li W, Zhang Y, Wu T, Cao J, Chen Z and Guan J 2019 *Results in Physics* **12** 1964
[27] Ma Q, Shi C B, Bai G D, Chen T Y, Noor Ahsan and Cui T J 2017 *Advanced Optical Materials* **5** 1700548
[28] Li J, Zhang Y T, Li J, Yan X, Liang, L J, Zhang Z, Huang J, Li J H, Yang Y and Yao J Q 2019 *Nanoscale* **11** 5746
[29] Ding G, Chen K, Luo X, Zhao J, Jiang T and Feng Y 2019 *Phys. Rev. Applied* **11** 044043
[30] Ding G W, Chen K, Jiang T, Sima B Y, Zhao J M and Feng Y J 2018 *Opt. Express* **26** 20990
[31] Qi Y P, Zhang Y, Liu C C, Zhang T, Zhang B H, Wang L Y, Deng X Y and Wang X X 2020 *Nanomaterials* **10** 533
[32] Xu K D, Li J, Zhang A and Chen Q 2020 *Opt. Express* **28** 11482
[33] Cen C, Zhang Y, Liang C, Chen X and Xiao S 2019 *Phys. Lett. A* **383** 3030
[34] Hu J G, Xie W Q, Chen J X, Zhou L M, Liu W, Li D M and Zhan Q W 2020 *Opt. Express* **28** 22095
[35] Hu J G, Yao E X, Xie W Q, Liu W, Li D M, Lu Y H and Zhan Q W 2019 *Opt. Express* **27** 18642
[36] Hu J G, Wu X H, Li H G, Yao E X, Xie W Q, Liu W, Lu Y H and Ming C G 2019 *J. Opt. Soc. Am. B* **36** 697
[37] Wang S, Wu P C, Su, V C, Lai Y C, Chen H C and Chen J W 2017 *Nat. Commun.* **8** 187
[38] Zeng J W, Huang F, Guclu C, Veysi M, Albooyeh M, Wickramasinghe H K and Capolino F 2018 *ACS Photonics* **5** 390
[39] Wan W, Gao J and Yang X 2017 *Advanced Optical Materials* **5** 1700541
[40] Beruete, Miguel and Irati Jáuregui-López 2020 *Advanced Optical Materials* **8** 3
[41] Zundel L and Manjavacas A 2017 *ACS Photonics* **4** 1831
[42] Banerjee S, Amith C S, Kumar D, Damarla G and Chowdhury D R 2019 *Opt. Commun.* **453** 124366
[43] Wan M L, He J N, Song Y L and Zhou F Q 2015 *Phys. Lett. A* **379** 1791
[44] Qiu L, Xiao G, Kong X and Xiong C 2019 *Opt. Express* **27** 21226
[45] Guo T J and Christos A 2016 *Opt. Lett.* **41** 5592
[46] Yu N F, Genevet P, Kats M A, Aieta F, Tetienne J P, Capasso F and Daburro Z 2011 *Science* **334** 333
[47] Liu S, Cui T J, Zhang L, *et al.* 2016 *Adv. Sci.* **3** 1600156
[48] Zhang L, Liu S, Li L L and Cui T J 2017 *ACS Appl. Mater. Interfaces* **9** 36447
[49] Li Y F, Zhang J Q, Qu S B, Wang J F, Chen H Y, Zheng L Xu Z and Zhang A X 2014 *J. Phys. D: Appl. Phys.* **47** 425103
[50] Allen L, Beijersbergen M W, Spreeuw R J C and Woerdman J P 1992 *Phys. Rev. A* **45** 8185
[51] Wang L, Liu S, Kong X, Wen Y and Liu X 2019 *Electron. Lett.* **55** 1168
[52] Chen P, Ge S J, Duan W, Wei B Y, Cui G X and Hu W 2017 *ACS Photonics* **4** 1333